Pharmaceutical Sciences and Drug Design
ISSN: 3062-4428
2022, Volume 2, Page No: 225-244

Available online at: www.galaxypub.co/page/journals

Galaxy Publication

Synthesis of Chalcone Derivatives as Anti-Inflammatory Agents and Investigation of Their Conformational Characteristics Using Nuclear Magnetic Resonance Spectroscopy and Molecular Modeling

Yuki Sato[1], Kenji Mori[2], Aiko Tanaka[1]*, Hiroshi Nakamura[2]

[1]Department of Medicinal Chemistry, Graduate School of Pharmaceutical Sciences, University of Tokyo, Tokyo, Japan.
[2]Department of Pharmaceutical Innovation, Faculty of Pharmaceutical Sciences, Osaka University, Osaka, Japan.

***E-mail** ✉ aiko.tanaka@outlook.com

Received: 08 January 2022; **Revised:** 11 March 2022; **Accepted:** 11 March 2022

ABSTRACT

This investigation involved the design and preparation of two chalcone analogues using both computational and laboratory approaches, evaluating their capacity to suppress lipoxygenase (LOX), an enzyme involved in inflammatory processes. The work builds upon prior studies where various chalcone derivatives were prepared and structurally confirmed. Here, we describe the repeated synthesis of two selected chalcones, emphasizing computational docking analyses, NMR spectroscopic examinations, and molecular dynamics simulations. Structural assignment for each compound was achieved by integrating data from Nuclear Magnetic Resonance (NMR) spectroscopy and Density Functional Theory (DFT) calculations. Additionally, the influence of substituents on the UV-visible absorption profiles of these chalcone analogues was explored. Docking predictions of LOX–chalcone complexes were subjected to molecular dynamics (MD) simulations to assess their binding stability. Following comprehensive in silico evaluation of the LOX–chalcone interactions, detailed atomic-level binding information for each analogue with 15-LOX-1 and 5-LOX was obtained via Saturation Transfer Difference (STD) NMR experiments. The compounds' selectivity was further evaluated against human 15-LOX-1 and broad lipoxidase enzymatic activity. Computational findings indicate that these chalcones represent potential lead structures for developing therapeutics aimed at lipoxygenase inhibition.

Keywords: Chalcones, Inflammation, LOX, NMR, Molecular dynamics

How to Cite This Article: Sato Y, Mori K, Tanaka A, Nakamura H. Synthesis of Chalcone Derivatives as Anti-Inflammatory Agents and Investigation of Their Conformational Characteristics Using Nuclear Magnetic Resonance Spectroscopy and Molecular Modeling. Pharm Sci Drug Des. 2022;2:225-44. https://doi.org/10.51847/jlDLwcL1lN

Introduction

Chalcones constitute a significant and diverse class of naturally occurring compounds belonging to the flavonoid family. They are characterized by an open-chain framework in which two aromatic rings (designated as A and B) are joined via an α,β-unsaturated carbonyl system **(Scheme 1).** These compounds demonstrate a wide range of biological activities, including antioxidant, antidiabetic, anti-inflammatory, neuroprotective, antiviral, antimalarial, antimicrobial, and antifungal properties [1-6].

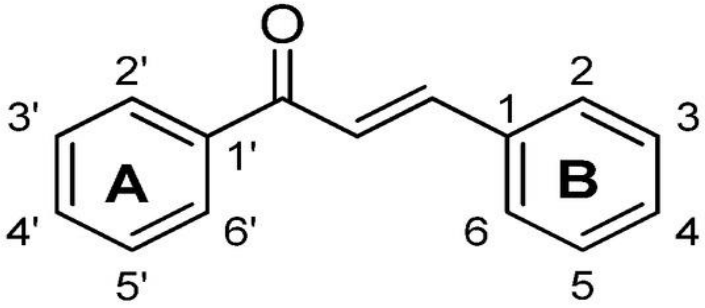

Scheme 1. General structure and numbering system of chalcones.

Chalcones have been widely employed as scaffold compounds in medicinal chemistry for the development of novel therapeutic agents, with evidence indicating that unsubstituted hydroxyl groups on both aromatic rings A and B are critical for enhancing their pharmacological effects [4].

2'-Hydroxychalcones are distinguished by the presence of a hydroxyl group (-OH) at the 2-position of ring A. This functional group significantly affects the physicochemical characteristics and bioactivity profiles of these molecules [7]. Extensive research on 2'-hydroxychalcones has explored their diverse therapeutic potentials, including anti-inflammatory [6, 8], anticancer [9], and antioxidant [3, 4, 7] activities, along with their capacity to inhibit lipoxygenases (LOXs) [3, 4]. Compounds demonstrating LOX inhibitory effects are recognized as promising candidates for pharmacological development.

Lipoxygenases (LOXs) are iron-dependent enzymes present in both plant and animal systems. They facilitate the dioxygenation of polyunsaturated fatty acids—such as arachidonic acid in mammals and linoleic acid in plants—producing hydroperoxide derivatives. Inhibitors of LOX attract considerable attention owing to their association with numerous pathophysiological states, positioning LOX as an attractive target for structure-based drug design and the identification of new therapeutic agents across a range of diseases. Furthermore, lipoxygenase enzymes contribute importantly to various normal and disease-related processes by converting polyunsaturated fatty acids into signaling lipid mediators. These products are involved in inflammatory responses, tumor development, and cardiovascular pathologies. Consequently, blocking LOX function offers potential benefits in alleviating inflammation, suppressing cancer progression, and countering oxidative damage. Insights into LOX mechanisms in these pathways support the rational design of selective inhibitors for managing associated conditions [3, 10, 11].

Building on earlier reports that demonstrated the inhibitory effects of several 2'-hydroxychalcones against soybean LOX [3, 4, 12], the present study selected two 2'-hydroxychalcones bearing 4-methyl and 4-chloro substituents on ring B **(Scheme 2),** chalcones 1 and 2) for re-synthesis using an improved protocol. These compounds were subjected to detailed investigation through integrated NMR spectroscopic techniques and computational modeling approaches.

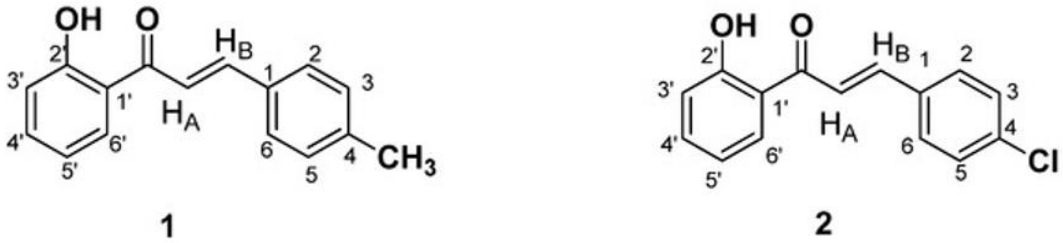

Scheme 2. Chemical structures of chalcones 1 and 2.

The investigations were performed to explore how various structural features might influence the inhibitory effects on LOX-1, LOX-5, and LOX-15 enzymes. Previous reports indicate that the potency of 2′-hydroxy-chalcones can be improved by adding groups like chloro or methyl at the 4-position of ring B [13]. Therefore, to examine the impact of substituents on ring B, two chalcones featuring distinct groups at the 4-position of this ring were

prepared in this work. In particular, chalcone 1 includes an electron-donating methyl substituent at the 4-position of ring B, whereas chalcone 2 has an electron-withdrawing chlorine atom in the identical position.

The binding characteristics of these chalcones with lipoxygenases were investigated using Saturation Transfer Difference (STD) NMR spectroscopy, along with molecular docking and molecular dynamics computations. Density functional theory (DFT) methods were employed for conformational studies. In addition, the inhibitory effects of the prepared chalcones against LOX-1 and LOX-15 were assessed in vitro.

Such research is valuable for evaluating the capacity of these molecules to interact with and maintain stability in the enzyme's binding pocket. Moreover, the outcomes from this study may offer deeper insights for the development of novel chalcones with improved lipoxygenase inhibitory properties.

Materials and Methods

General synthetic protocol for chalcone preparation

The 2'-hydroxychalcones 1 and 2 **(Scheme 2)** were obtained through Claisen–Schmidt condensation of 2-hydroxyacetophenone with the corresponding benzaldehydes under alkaline conditions, following a reported method [3].

In detail, an equimolar mixture of 2-hydroxyacetophenone and the selected benzaldehyde was dissolved in ethanol, followed by addition of 20% w/v aqueous KOH. The reaction was allowed to proceed with stirring at ambient temperature for 24 h. Subsequently, the mixture was cooled to 0 °C and neutralized with 10% aqueous HCl, leading to precipitation of a yellow solid that was collected by filtration and rinsed with dilute HCl. Final purification was achieved by recrystallization.

All reagents employed in chalcone synthesis were acquired from Sigma-Aldrich (Burlington, MA, USA), Fluka (Buchs, Switzerland), Alfa-Aesar (Lancashire, UK), or Acros (Fukuoka, Japan) and used as received. Reaction progress was tracked using thin-layer chromatography on Macherey-Nagel (Düren, Germany) plates (0.20 mm silica thickness).

Compound 1 (2'-hydroxy-4-methylchalcone) was synthesized according to the general protocol using 2-hydroxyacetophenone (265 µL, 2.20 mmol) and 4-methylbenzaldehyde (259 µL, 2.20 mmol) in 5.4 mL ethanol, with 1.8 mL of 20% aqueous KOH. Recrystallization from hexane/ethyl acetate afforded the product as a yellow solid. Yield: 385.4 mg (70%). Melting point: 117–119 °C (lit. [3] 116–117 °C).

^{1}H NMR (400 MHz, $CDCl_3$): δ (ppm) 12.90 (s, 1H, OH), 7.95 (m, 2H, H6′ & Hβ), 7.65 (d, 1H, J = 15.4 Hz, Hα), 7.59 (d, 2H, J = 8.0 Hz, H2 & H6), 7.52 (ddd, 1H, J = 8.6, 7.2, 1.6 Hz, H4′), 7.27 (d, 2H, J = 8.6 Hz, H3 & H5), 7.05 (dd, 1H, J = 8.4, 1.2 Hz, H3′), 6.97 (ddd, 1H, J = 7.87, 0.73 Hz, H5′), 2.42 (s, 3H, $–CH_3$).

Compound 2 (2'-hydroxy-4-chlorochalcone) was prepared similarly from 2-hydroxyacetophenone (354 µL, 2.94 mmol) and 4-chlorobenzaldehyde (413.2 mg, 2.94 mmol) in 7.2 mL ethanol, treated with 2.4 mL of 20% aqueous KOH. The product was isolated by recrystallization from methanol as a yellow-orange solid. Yield: 620.4 mg (78%). Melting point: 148–151 °C (lit. [3] 153–156 °C).

^{1}H NMR (400 MHz, $CDCl_3$): δ (ppm) 12.75 (s, 1H, OH), 7.91 (d, 1H, J = 8.0 Hz, H6′), 7.87 (d, 1H, J = 15.5 Hz, Hβ), 7.65–7.59 (m, 3H, H2, H6 & Hα), 7.51 (t, 1H, J = 7.8 Hz, H4′), 7.42 (d, 2H, J = 8.1 Hz, H3 & H5), 7.04 (d, 1H, J = 8.4 Hz, H3′), 6.95 (t, 1H, J = 7.6 Hz, H5′).

Structural elucidation

Structural confirmation of both compounds was performed using 600 and 850 MHz Bruker Avance spectrometers located at the National and Kapodistrian University of Athens, the National Institute of Chemistry (Ljubljana), and the University of Helsinki. This included one- and two-dimensional homo- and heteronuclear NMR techniques drawn from the instrument's standard pulse program library. Spectra were processed and analyzed with MestreNova (Santiago de Compostela, Spain) and TopSpin 4.2.0 software [14-18].

Saturation transfer difference (STD) NMR spectroscopy

Samples for STD NMR were prepared by initially dissolving the chalcones in DMSO-d_6, then diluting with 20 mM potassium phosphate buffer (pH 7.2) in D_2O to a final volume of 600 µL. Chalcone 1 required 192 µL DMSO, while chalcone 2 required 206 µL. Stock solutions were made by dissolving compound 1 in 310 µL DMSO and compound 2 in 250 µL DMSO. In the NMR tube, final concentrations were 1000 µM ligand and 1 µM enzyme, giving a 1:1000 protein-to-ligand ratio. Experiments were conducted at 25 °C. Human 5-lipoxygenase and 15-

lipoxygenase-1 were selected for these binding studies owing to their physiological importance, differing biological functions, and the availability of stable enzyme samples appropriate for interaction analysis [2, 19-21]. STD NMR data were acquired on a Bruker AV 850 MHz spectrometer (Bruker Biospin, Rheinstetten, Germany) using TopSpin 2.1. The sweep width was 13,586.957 Hz. Standard Bruker pulse programs were employed. On-resonance saturation was applied at 4.7 ppm for 2 s (using 16 cycles), while off-resonance irradiation for the control spectrum was set at 12.68 ppm.

Computational conformational study

Conformational searches were performed employing density functional theory (DFT) [22] at the BP86/def2-SVP level [23, 24]. This methodology, recognized for its reliability, included full geometry optimization of all conformers followed by frequency calculations to verify that they corresponded to true energy minima on the potential energy surface. Multiple starting conformations for each compound were generated through systematic variation, focusing on rotations around the -OH, -Ph, and -CH_3 groups, as well as consideration of trans–cis isomerism. The global minimum-energy conformer was identified, and its UV–vis absorption and emission properties were theoretically evaluated as described later. The computed structural parameters were subsequently compared to experimental data derived from NMR spectroscopy. All quantum chemical computations were executed in the gas phase using the ORCA 4.0.1 program [25].

Induced fit docking simulations

Induced fit docking protocols were applied to investigate possible binding modes of the ligands within the active sites of LOX-1, 15-LOX, and 5-LOX enzymes. These targets were selected based on literature evidence indicating that chalcone scaffolds can effectively inhibit lipoxygenases [14, 26], supplemented by target prediction results from the Swiss Target Prediction tool, which highlighted LOX enzymes as probable interactors for both compounds. The X-ray crystal structures employed were PDB entries 5T5V [27], 2P0M [28], and 3O8Y [29]. Protein structures were prepared using the Protein Preparation Wizard module within the Schrödinger Suite. To properly handle the metalloprotein nature of LOX enzymes, the catalytic Fe^{3+} ion was treated by creating zero-order bonds to coordinating residues via the dedicated tool in Maestro, thereby disrupting original bonds, establishing new zero-order interactions, and adjusting formal charges to match the crystallographically observed coordination environment.

The ligand molecules were constructed using the 2D/3D builder in Maestro 2017-1 (Schrödinger) and subjected to energy minimization with MacroModel (version 10) [30] as well as DFT optimizations integrated in the Schrödinger platform. This dual approach ensured robust low-energy conformers via quantum mechanics while allowing efficient refinement within the binding pocket using molecular mechanics. Ligand 3D structures were generated with LigPrep, accounting for possible stereoisomers and selecting the “add metal binding states” feature to facilitate coordination. Geometry optimizations in MacroModel preserved stereochemical integrity. The OPLS2005 force field [31] was applied for minimizations, with ionization states assigned at physiological pH. Accurate 3D coordinates were produced incorporating Hammett–Taft correlations and ionization penalties. Solvent effects were modeled implicitly with water during ligand minimization under OPLS2005. Low-energy conformers were explored via a combined torsional/low-mode sampling search, and the most stable structure was chosen for docking.

Docking was conducted using the Induced Fit Docking (IFD) workflow in the Schrödinger Suite, incorporating five low-energy ligand conformers from MacroModel. Grid centers were defined by key active-site residues: for 5T5V, ILE839, HIS499, HIS504, HIS690, and ASN694; for 3O8Y, ASN407, HIS432, ILE673, HIS367, HIS372, and HIS550; for 2P0M, ILE663, HIS545, ILE400, LEU597, ILE593, and VAL409. Protein preparation prior to docking included restrained refinement, automatic side-chain trimming guided by B-factors, and Prime-based side-chain optimization. Glide XP docking was performed with a dielectric constant of 80 for the binding site, retaining crystallographic water molecules throughout the procedure.

Molecular dynamics simulations

Molecular dynamics (MD) trajectories [32] were generated with the protein–ligand complexes solvated in explicit SPC/E water. The systems were neutralized by adding Na^+ and Cl^- ions to achieve a physiological salt concentration of 0.150 M NaCl. The protein N-terminus was capped with an acetyl group, whereas the C-terminus remained uncapped given its proximity to the active site. All simulations employed the OPLS2005 force field for

describing protein–ligand interactions. Long-range electrostatics were treated with the particle mesh Ewald (PME) method [33, 34] using a 0.8 Å grid spacing. Short-range electrostatic and van der Waals interactions were cut off smoothly at 9.0 Å. Thermodynamic control was achieved with the Nosé–Hoover thermostat [35] for temperature and the Martyna–Tobias–Klein barostat [34] for pressure. Periodic boundary conditions were enforced with a simulation box buffered by 10.0 × 10.0 × 10.0 Å around the solute.

Integration of equations of motion utilized the RESPA multiple-time-step algorithm [36], with a 2 fs inner step for bonded and short-range non-bonded forces, and a 6 fs outer step for long-range non-bonded interactions beyond the cutoff. Systems were equilibrated following the standard Desmond relaxation protocol [37], starting with restrained Brownian dynamics in the NVT ensemble at 310 K, followed by unrestrained NPT equilibration for 1.0 ns. Production MD runs were then extended to 200 ns to accumulate statistically reliable data on ligand binding stability within the enzyme pocket. Simulations were executed on GPU-accelerated workstations using Desmond, and trajectory quality was assessed by monitoring RMSD convergence of the protein Cα backbone and the bound ligand.

Computed absorption and fluorescence spectra

Theoretical UV–vis absorption and fluorescence spectra were obtained via time-dependent DFT (TD-DFT) at the BP86/def2-SVP and B3LYP [38, 39]/def2-SVP levels. Absorption spectra were calculated for 10 singlet excited states of the isolated molecules (optimized at the ground-state DFT geometry) and for snapshots extracted from MD simulations of the complexes with 5-LOX and 15-LOX-1. Emission spectra were derived from geometry optimizations in the first and second excited states. The B3LYP functional was selected for its established performance in reproducing absorption and emission wavelengths [40]. All quantum calculations and spectral visualizations were performed with Gaussian 16 [41] and ORCA software packages.

Assessment of binding free energies via molecular mechanics/generalized born surface area (MM/GBSA)

The binding stability of the protein-ligand assemblies was assessed employing the MM/GBSA technique, which estimates the free energy of binding [42]. This methodology was applied to the complex models through the Prime tool within Maestro software release 2024-4. The MM/GBSA computations targeted the three ligand-protein assemblies deemed most representative based on clustering from a molecular dynamics simulation trajectory. Protein flexibility was accounted for using the VSGB solvation approach, valued for its accurate treatment of solvation effects, along with the OPLS-2005 force field. The binding free energy was determined according to the equation:

$$\Delta G\_bind = E\_complex\ (minimized) - E\_ligand\ (minimized) - E\_receptor\ (minimized). \quad (2)$$

Assays for enzyme inhibition

Enzyme activity measurement: Human 15-LOX1 (h-15LOX1) was produced in BL21 (DE3) Escherichia coli cells, and the resulting cell lysate served as the enzyme source for the activity tests, following previously reported protocols [43-45]. In summary, the enzymatic transformation of linoleic acid into 13S-hydroperoxy-9Z,11E-octadecadienoic acid (13(S)-HpODE) was monitored by tracking UV absorbance at 234 nm as a function of time, utilizing a ThermoFisher Varioskan Plate Reader in Greiner Bio-One F-bottom 96-well plates. Data collection spanned 20 minutes with readings every 20 seconds. Only the initial linear phase, generally the first 1–5 minutes (varying with enzyme amount), was considered for calculating activity rates, as the reaction velocity decreased afterward due to substrate depletion. This assay helped establish the ideal lysate dilution (×200 in assay buffer: 50 mM HEPES, 50 mM NaCl, pH 7.5). Linoleic acid (Sigma Aldrich, L1376) was prepared in ethanol. An identical procedure was followed to optimize the concentration of commercial soybean lipoxygenase (Sigma Aldrich, Burlington, MA, USA; L7395), diluted ×16,000 in assay buffer (50 mM Tris, 50 mM NaCl, pH 7.5).

Inhibitor screening via UV-based assay: Inhibitory effects of the tested molecules were evaluated using the same UV monitoring method for 13(S)-HpODE formation at 234 nm. Compounds were initially prepared in DMSO to reach 4 mM stock solutions, then further diluted in assay buffer for testing at 100 μM final concentration. Each candidate was pre-incubated for 10 minutes at room temperature with the appropriately diluted cell lysate or soybean lipoxygenase before adding linoleic acid (25 μM final). Activity levels were expressed relative to inhibitor-free controls set at 100%. Molecules reducing enzyme activity below 50% were classified as active hits.

Experiments were conducted in triplicate, with data analysis performed using Microsoft Excel Professional Plus 2021 and GraphPad Prism version 9.0.0.

Results and Discussion

Confirmation of the structures of chalcones 1 and 2

Structural assignment for chalcone 1 began with the identification of the doublets at 7.83 and 8.05 ppm, assigned to protons Hα and Hβ, consistent with prior literature descriptions [3]. Using 2D-NOESY experiments, protons H2 and H3 were assigned, and a correlation was noted between Hβ and H2. The attached carbons were determined via 2D-HSQC, based on direct 1JC-H couplings. A NOESY correlation was detected between Hα and a signal at 8.25 ppm, identified as H6′ due to its proximity and doublet splitting from coupling to a single adjacent proton. Starting from H6′, the other aromatic protons were assigned through further NOESY interactions. Corresponding carbons were linked via 2D-HSQC using one-bond couplings. The 13C-1H 2D HSQC spectrum allowed assignment of all protonated carbons, while quaternary and carbonyl carbons were identified through 13C-1H 2D HMBC. Key observations included a 2JC-H correlation from Hα to C1, a 3JC-H from H2 to C4, and from H6′ both a 3JC-H to C2′ and a 2JC-H to C1′. This methodical process enabled full assignment of all protons and carbons in chalcone 1.

An analogous approach was applied to chalcone 2. Spectra for both compounds were recorded in DMSO-d6. The 1H NMR spectra are displayed in **Figure 1**, and the assigned chemical shifts for the two molecules are listed in **Table 1.**

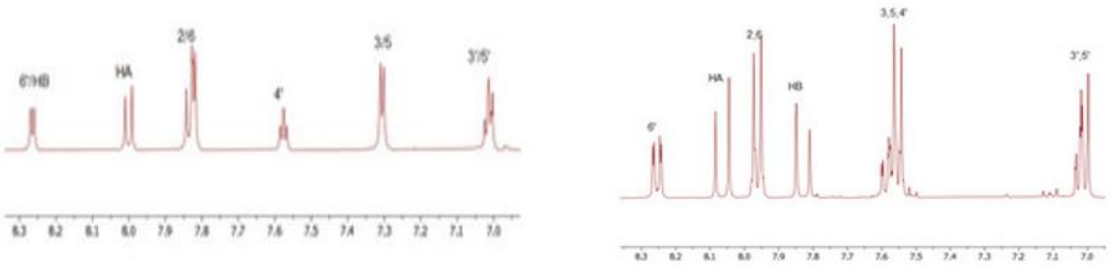

a) b)

Figure 1. 1H NMR spectra of compounds (a) 1 and (b) 2 recorded in DMSO-d6. The spectra were acquired on a Bruker AC 850 MHz instrument at 25 °C.

Table 1. Assignment of the experimental ^{1}H NMR spectra of **1** and **2** in DMSO-d_6.

Hydrogen 1	**Chemical Shift (ppm)**	**Hydrogen 1**	**Chemical Shift (ppm)**	**Hydrogen 1**	**Chemical Shift (ppm)**
CH_3	2.36	HA	8.01	5’	6.96
2.6	7.82	HB	8.25	4’	7.57
3.5	7.29	3’	7.05	6’	8.27
OH	12.56				
Hydrogen 2	**Chemical Shift (ppm)**	**Hydrogen 2**	**Chemical Shift (ppm)**	**Hydrogen 2**	**Chemical Shift (ppm)**
2.6	7.96	HB	7.83	4’	7.58
3.5	7.55	3’	7.01	6’	8.25
H_A	8.05	5’	7.01		
OH	12.43				

Conformational analysis findings

Density functional theory (DFT) calculations were utilized to determine the minimum-energy conformations of chalcones 1 and 2, selected for their superior accuracy relative to alternative computational approaches. A series of initial geometries were subjected to full optimization, resulting in eight distinct conformers for each molecule. Following identification of the lowest-energy conformer, interproton distances corresponding to the spatial correlations observed in the 2D-NOESY experiments were computed. These calculated distances confirmed the close proximity of the relevant protons, thereby supporting the experimentally detected NOE signals.

Integration of the relative energy values, structural features, and NOESY correlation data led to the conclusion that the conformations shown in panels (a) and (b) most accurately represent the predominant forms of chalcones 1 and 2, respectively.

The computational results align best with a trans configuration of the enone system, consistent with the experimental observations. Comparison of the preferred conformations of the two compounds **(Figure 2)** reveals a key difference in the relative orientation of the carbonyl and phenolic hydroxyl groups. In the minimum-energy structure of chalcone 1, the carbonyl oxygen is directed away from the hydroxyl group, adopting an anti-periplanar arrangement. In contrast, the lowest-energy conformation of chalcone 2 positions the carbonyl oxygen toward the phenolic hydroxyl, enabling the formation of an intramolecular hydrogen bond.

Table 2 lists the proton pairs exhibiting NOESY correlations for both compounds, together with the corresponding calculated interproton distances.

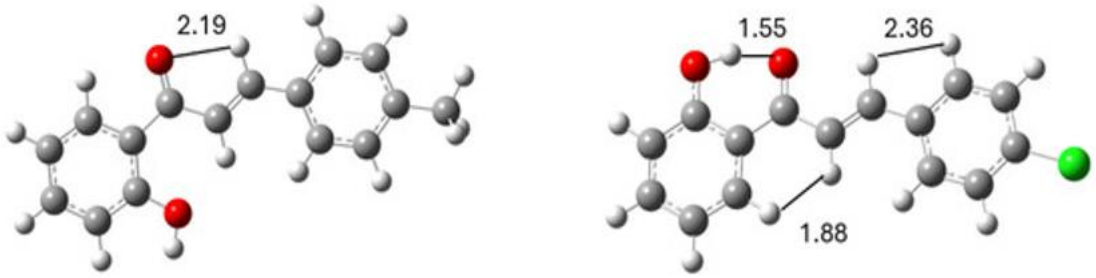

a) b)

Figure 2. Minimum-energy conformations of (a) compound 1 and (b) compound 2, highlighting the key spatial proton–proton correlations that support the assignment of these structures as the predominant forms; interproton distances (in Å) computed at the DFT (BP86/def2-SVP) level (oxygen atoms shown in red, chlorine in green).

Table 2. Table of signals observed in 2D-NOESY, along with their measured distances.

Observed Signal in 2D-NOESY Spectrum	Distance in Å
1	
H2-HB	2.192
2	
H2-HB	2.363
H6'-HA	1.882

Molecular docking studies

Induced fit docking (IFD) was performed using the Glide/XP protocol to generate a range of binding poses for chalcones 1 and 2 within the active sites of LOX-1, 15-LOX, and 5-LOX. The resulting protein–ligand complexes were ranked according to the descending order of their IFD Scores **(Table 3)**. This composite scoring function accounts for both the binding affinity of the ligand in the protein pocket and the Prime energy contribution from the protein conformation across all evaluated complexes.

Table 3. Docking results between the molecules and macromolecules in kcal/mol.

Compound	IFD Score (5-LOX)	IFD Score (LOX-1)	IFD Score (15-LOX)
1	−10.778	−9.657	−7.581
2	−11.630	−10.256	−7.634

The conformers exhibiting the lowest energy were chosen as the representative docking poses for the subsequent molecular dynamics (MD) simulations. These poses were selected due to their direct engagement of the ligand with the enzyme active site, coupled with the most favorable IFD scores, which signify the highest stability of the resulting protein–ligand complexes. Furthermore, the conformers within this top-ranked cluster displayed negligible differences in binding energies and overall binding modes.

Analysis of the computed binding energies indicates that both compounds are expected to interact robustly with the active sites of 5-LOX and LOX-1. In particular, compound 1 is predicted to establish three hydrogen bonds involving its hydroxyl and carbonyl groups with the ASN425 residue in 5-LOX, along with two π–π stacking interactions with HIS367 and HIS372 **(Figure 3).** Within LOX-1, compound 1 engages in two π–π stacking contacts with HIS504 and TRP500. For compound 2, docking results suggest the formation of two hydrogen bonds between its carbonyl oxygen and HIS367 in 5-LOX, accompanied by two π–π interactions with HIS372 and PHE421 **(Figure 4).** In LOX-1, compound 2 shows one π–π interaction with TRP500.

In contrast, neither compound demonstrates strong binding to the active site of 15-LOX. Compound 1 is proposed to form two π–π interactions with HIS361 and HIS366, while compound 2 exhibits only one such interaction with HIS361 **(Figure 5).** This limited affinity explains why STD NMR experiments were not pursued for 15-LOX.

All specific interactions between the two chalcones and the lipoxygenase enzymes are summarized in **Table 4.**

The present investigation demonstrates that the chalcones under study display markedly superior inhibitory potency toward LOX-1 relative to previously reported analogs. This enhanced activity is attributable to more favorable engagement with the LOX-1 binding pocket, presumably arising from their distinctive structural characteristics. Consequently, these compounds hold promising potential as therapeutic candidates for pathways involving LOX-1 [46].

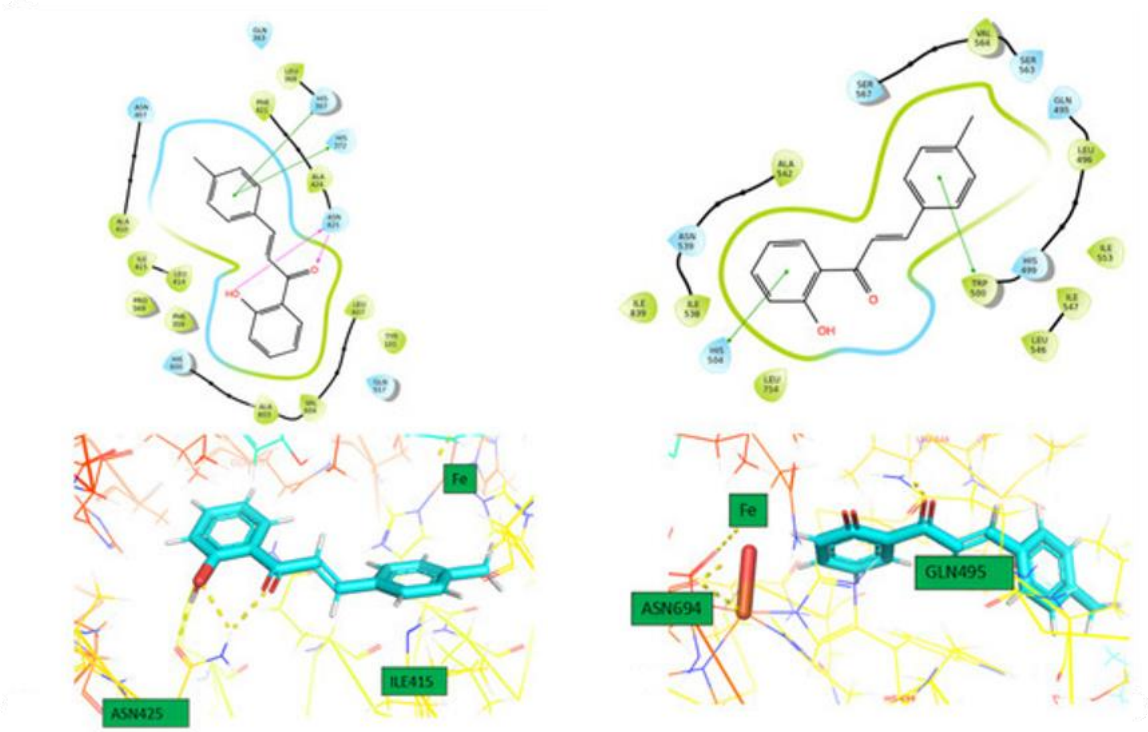

a) b)

Figure 3. Binding interactions of compound 1 with (a) 5-LOX and (b) LOX-1, depicted in 2D representation (top) and 3D representation (bottom).

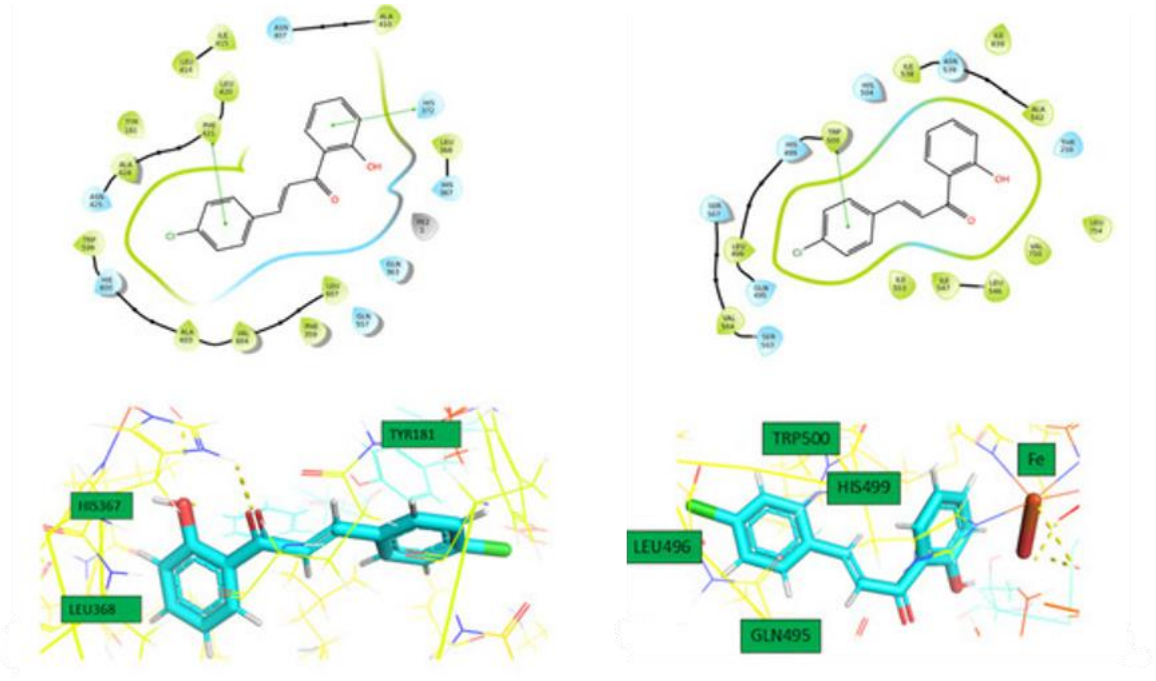

a) b)

Figure 4. Binding interactions of compound 2 with (a) 5-LOX and (b) LOX-1, depicted in 2D representation (top) and 3D representation (bottom).

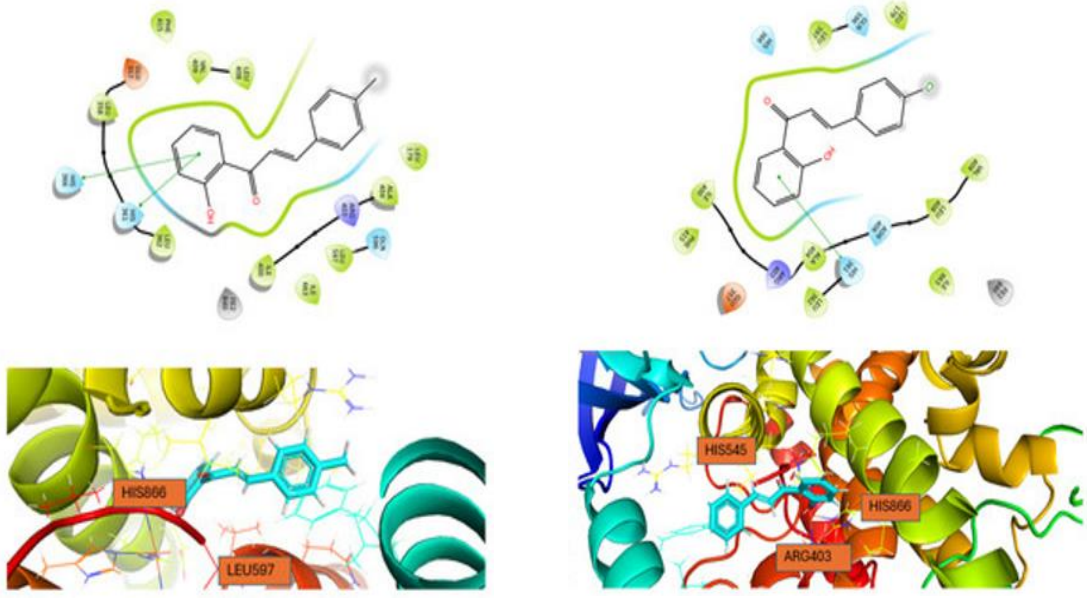

a) b)

Figure 5. Binding interactions of (a) compound 1 with 15-LOX and (b) compound 2 with 15-LOX, shown in 2D representation (top) and 3D representation (bottom).

Table 4. Interactions of the molecules with the enzymes.

Compound	Enzyme	Hydrogen Bonds	π-π Stacking
1	5-LOX	ASN425	HIS367, HIS372
	LOX-1		HIS504, TRP500
	15-LOX		HIS361, HIS366
2	5-LOX		HIS372, PHE421
	LOX-1		TRP500
	15-LOX		HIS361

Molecular dynamics simulation results

Molecular dynamics (MD) simulations were performed to evaluate the stability of the binding poses proposed by the docking studies. The MD trajectories of the protein–ligand complexes revealed consistent retention of both compounds within the active site cavities of the LOX enzymes. To assess this stability quantitatively, the root-mean-square deviation (RMSD) of each ligand was monitored relative to its initial docked conformation.

Throughout the 200 ns simulations, both ligands remained firmly bound within the binding pockets of the respective enzymes. This persistent occupancy supports the reliability of the docking predictions and suggests that these chalcones could effectively function as LOX inhibitors with promising therapeutic potential.

Figure 6 illustrates the RMSD profiles: the Cα atoms of the protein exhibit low RMSD values (<4.0 Å), confirming good conformational convergence of the system, while the ligand RMSD is also shown over the full 200 ns trajectory. Ligand RMSD was calculated using heavy atoms and referenced to the starting docking pose. Both compounds displayed excellent stability, maintaining RMSD values below approximately 4.0 Å across the simulation, as presented in **Figure 6**.

Analysis of the interaction timeline further indicated that the number of protein–ligand contacts remained largely constant for both compounds, with only minor fluctuations reflecting dynamic binding behavior. For compound 1, residues such as TYR181, LEU420, and PHE421 formed persistent and robust interactions, highlighting their critical role in ligand stabilization. Other residues, including GLN363, LEU414, and ASN425, showed more sporadic contacts, likely due to transient interactions or local flexibility.

In compound 2, the interaction heatmap revealed variability in contact patterns: certain residues (e.g., HIS372 and HIS603) maintained steady engagement, whereas others (e.g., VAL604 and ILE673) displayed short-lived but intense interactions.

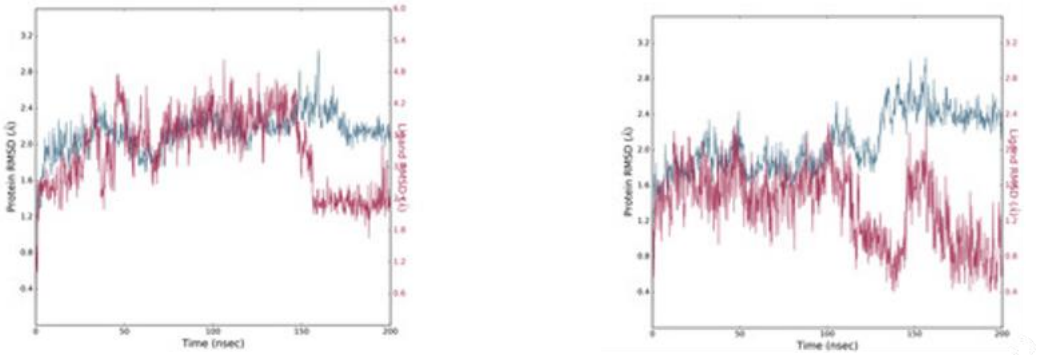

a) b)

Figure 6. Root-mean-square deviation (RMSD) profiles for the protein backbone (5-LOX, shown in green) and the ligands (a) compound 1 and (b) compound 2 (shown in magenta) over the course of a 200 ns molecular dynamics simulation, using the initial docking pose as the reference structure (top panel).

In **Figure 7**, the Cα atoms of the protein display low RMSD values (<4.0 Å), confirming effective system convergence, while the ligand RMSD is presented across the entire 200 ns MD trajectory. Ligand RMSD was determined based on heavy atoms relative to the starting docked conformation. Both ligands maintained excellent stability throughout the simulation, with RMSD values remaining below approximately 4.0 Å, as shown in **Figure 7**.

Additionally, the interaction timeline for compound 1 reveals moderate fluctuations in the number of contacts, varying between 6 and 12, indicative of a dynamically adaptable binding mode within the pocket. Persistent interactions were observed with key residues such as LEU496 and ILE553, underscoring their critical contribution to ligand stabilization. In contrast, contacts with residues like ALA542 and ILE839 were more intermittent and sporadic, suggesting areas of greater flexibility or transient engagement.

For compound 2, steady interactions were maintained with residues ILE839, HIS690, and ASN694, whereas contacts with ILE837 and ALA542 were more variable and occasional.

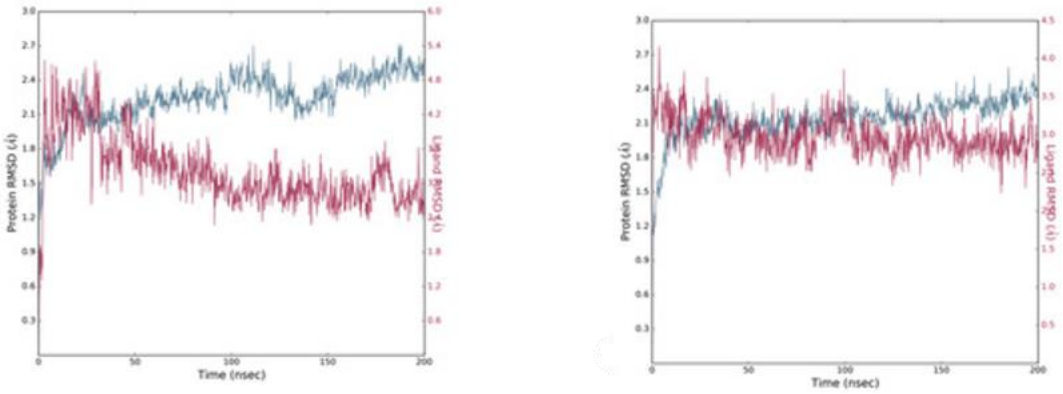

a) b)

Figure 7. Root-mean-square deviation (RMSD) profiles for the protein backbone (LOX-1, shown in green) and the ligands (a) compound 1 and (b) compound 2 (shown in magenta) over the course of a 200 ns molecular dynamics simulation, using the initial docking pose as the reference structure (top panel).

In **Figure 8,** the Cα atoms of the protein exhibit low RMSD values (<4.0 Å), confirming effective system convergence, while the ligand RMSD is presented across the full 200 ns MD trajectory. Ligand RMSD was calculated based on heavy atoms relative to the initial docked conformation. Both ligands demonstrated outstanding stability throughout the simulation, maintaining RMSD values below approximately 4.0 Å, as displayed in **Figure 8.**

Analysis of the interaction timeline indicates that compound 1 formed more persistent contacts with residues HIS541, ILE663, and HIS361 over the course of the simulation, whereas interactions with ILE593 and GLN596 were more intermittent. For compound 2, steady contacts were observed with HIS361, HIS541, and ILE663, while interactions with ILE414 and GLN548 were more variable and sporadic.

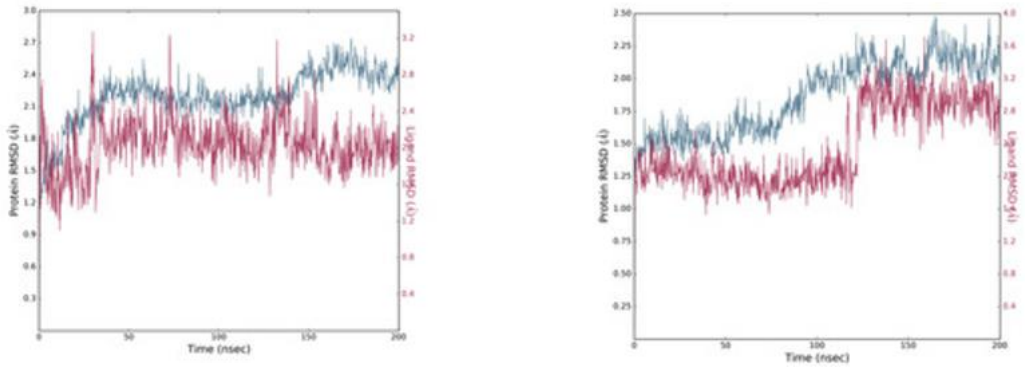

a) b)

Figure 8. Root mean square deviation (RMSD) profiles for the backbone of 15-LOX (shown in green) and for ligands 1 (panel a) and 2 (panel b) (shown in magenta) were determined throughout a 200 ns molecular dynamics trajectory, using the original docked conformation as the reference structure (top panel).

Mapping the binding epitopes of the compounds with LOX-1 and 5-LOX via saturation transfer difference (STD) NMR spectroscopy

Having confirmed the inhibitory activity of these compounds against LOX-1 and 5-LOX, we sought to explore their direct binding modes in greater detail and to identify the specific proton epitopes involved in the interaction with soybean LOX-1 and 5-LOX. For this purpose, we utilized Saturation Transfer Difference (STD) NMR spectroscopy, a powerful method for detecting ligand–target interactions and determining which protons of the small molecule are in close proximity to the binding pocket.

The STD NMR data illustrating the binding of the compounds to LOX-1 and 5-LOX are presented in **Figures 9 and 10**. Comparison of the STD spectra with the standard 1H NMR reference spectra shows a clear reduction in signal intensity for both aromatic and aliphatic protons of the ligands. This attenuation strongly supports the

existence of direct binding between the compounds and the two LOX isoforms. In particular, analysis of the aromatic region reveals that the majority of aromatic protons are involved in contacts with the protein's active site. The weaker signals observed in the STD spectra relative to the off-resonance reference (acquired in the absence of saturation) reflect efficient saturation transfer from the protein to the bound ligand, resulting in diminished peak intensities for protons in close contact. This pattern indicates robust and specific ligand–protein complex formation.

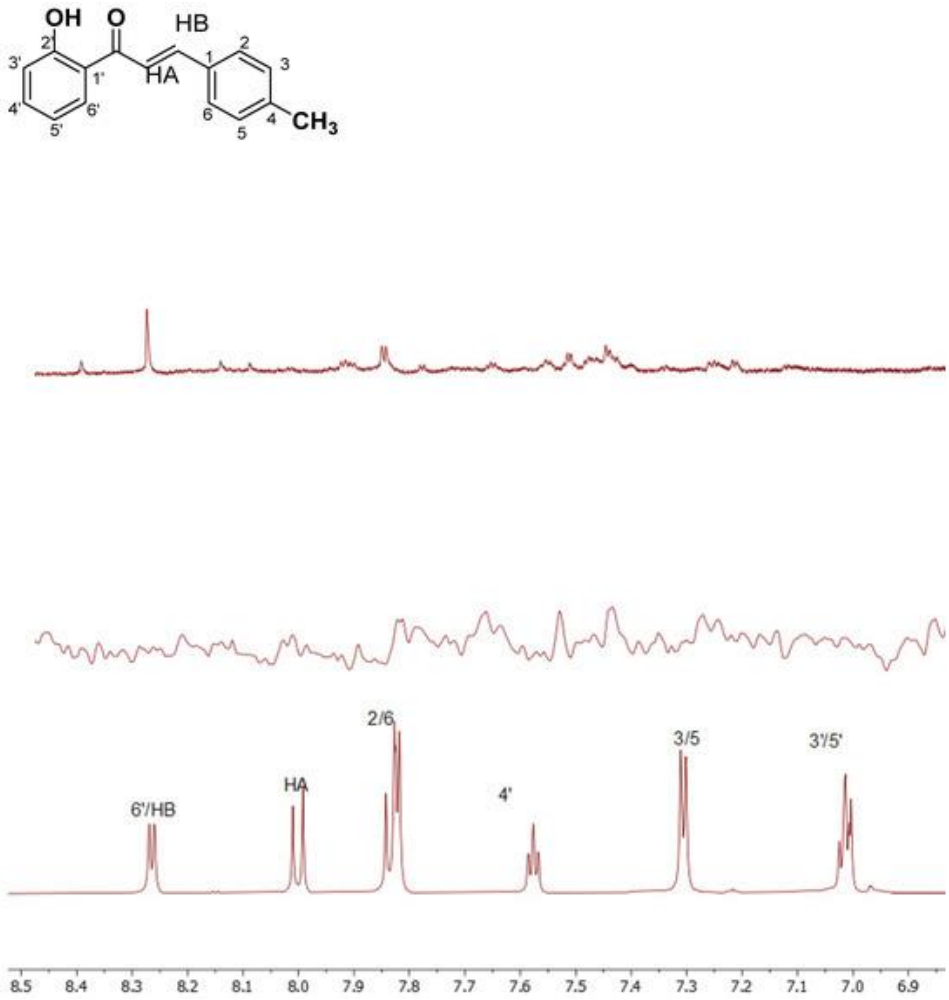

Figure 9. (Top) Off-resonance STD-NMR reference spectrum of compound 1 (1000 µM) in the presence of 5-LOX (1 µM), corresponding to a protein:ligand ratio of 1:1000, recorded in potassium phosphate buffer (pH 7.2) containing 600 µL D2O on an 850 MHz NMR spectrometer at 25 °C.
(Middle) Off-resonance STD-NMR reference spectrum of compound 1 (1000 µM) in the presence of soybean LOX-1 (10 µM), corresponding to a protein:ligand ratio of 1:100, acquired under the same buffer conditions (potassium phosphate, pH 7.2, 600 µL D2O) on an 850 MHz NMR spectrometer at 25 °C.
(Bottom) Standard 1H NMR spectrum of compound 1 in DMSO-d6, recorded on an 850 MHz NMR spectrometer at 25 °C.

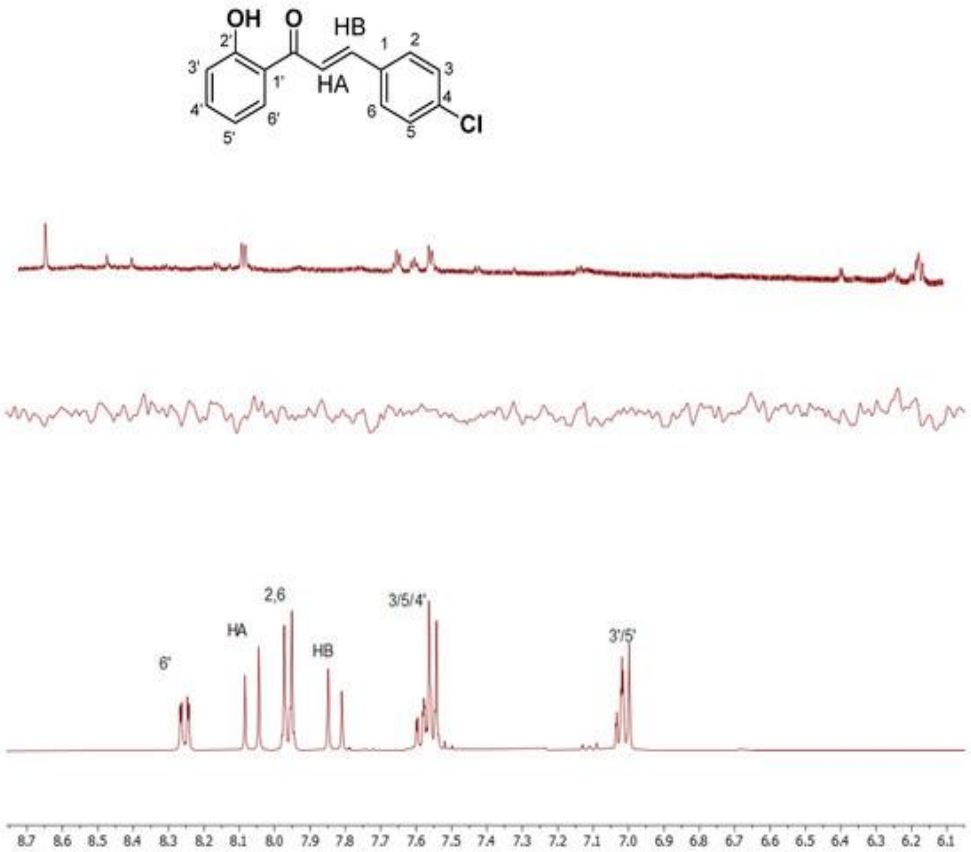

Figure 10. (Top) Off-resonance STD-NMR reference spectrum of compound 2 (1000 μM) in the presence of 5-LOX (1 μM), at a protein:ligand ratio of 1:1000, recorded in potassium phosphate buffer (pH 7.2) with 600 μL D2O on an 850 MHz NMR spectrometer at 25 °C.
(Middle) Off-resonance STD-NMR reference spectrum of compound 2 (1000 μM) in the presence of soybean LOX-1 (10 μM), at a protein:ligand ratio of 1:100, acquired in potassium phosphate buffer (pH 7.2) containing 600 μL D2O on an 850 MHz NMR spectrometer at 25 °C.
(Bottom) Standard 1H NMR spectrum of compound 2 in DMSO-d6, recorded on an 850 MHz NMR spectrometer at 25 °C.

These observations are consistent with our computational docking and dynamics studies, which indicated that the aromatic moieties of both compounds engage in interactions with 5-LOX. Specifically, for compound 1, the majority of aromatic protons from both rings displayed close contacts with 5-LOX, and a similar pattern was evident for compound 2. In contrast, with LOX-1, significant interactions were observed primarily for the aromatic protons of compound 1 **(Figure 9)**, (middle panel), where the corresponding STD spectrum revealed detectable signals. The limited aqueous solubility of the compounds in D2O likely restricted their effective dispersion and interaction in the buffer system, potentially diminishing the observable STD effects. Additionally, the absence or weakness of certain signals may reflect relatively modest binding affinities at the protein active site, as further corroborated by the in vitro inhibition data [47, 48].

Absorption and emission spectra

Table 5 lists the wavelength (λ) values, corresponding energy gaps, and oscillator strengths for the major transitions in the UV–visible absorption spectra of the unbound chalcone compounds and their enzyme-bound forms, as derived from molecular dynamics simulations. The absorption profiles are visualized in **Figure 11**.

Table 6 presents the wavelength (λ) values, energy differences, and oscillator strengths for the key bands in the UV–visible fluorescence emission spectra of the free chalcones and those complexed within the enzymes, computed from MD trajectories.

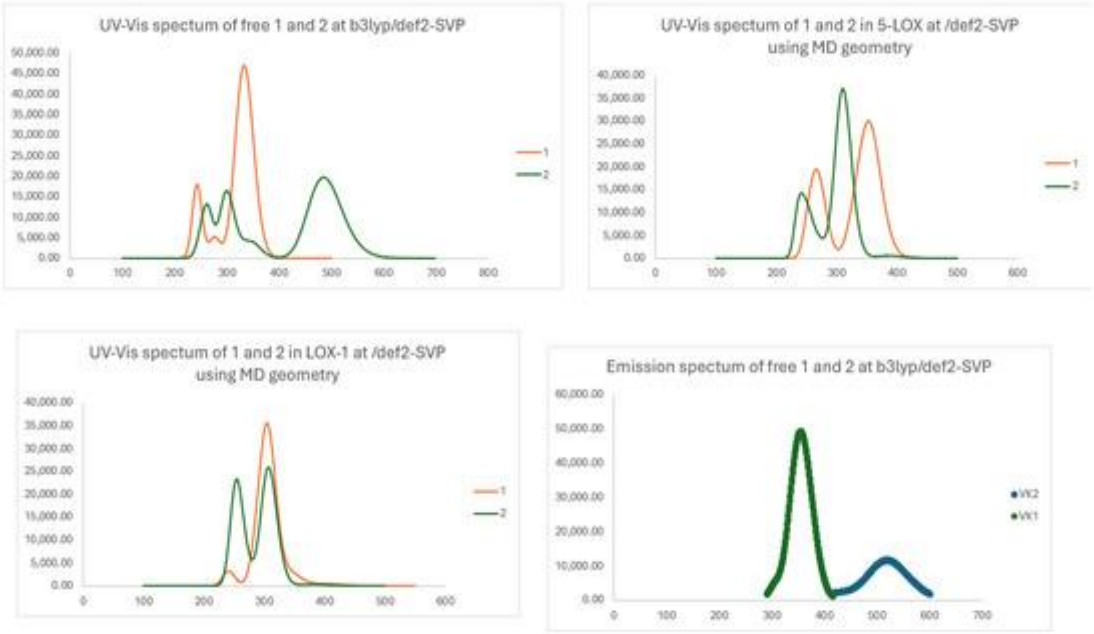

Figure 11. UV-Vis absorption profiles for the unbound computed molecules and their complexes when docked into 5-LOX and LOX-1, as determined with the B3LYP/def2-SVP approach. Fluorescence emission profiles for the unbound computed molecules, calculated using the same B3LYP/def2-SVP level of theory. Structural representations of the ligand–protein complexes following molecular dynamics simulations.

Table 5. Calculated wavelength λ (nm), energy difference ΔE (eV), and oscillator strength f for the primary excited states and selected UV–vis absorption transitions of the free compounds, as well as those encapsulated in LOX-5 and 1-LOX, computed at the B3LYP/def2-SVP level of theory.

	State	ΔE	λ	f
1	S_1	3.755	383.5	0.3485
1_LOX-1	S_1	3.076	403.1	0.0059
1_LOX-1	S_3	4.048	306.3	0.4806
1_5-LOX	S_1	3.215	385.6	0.0005
1-OCH_3[a]	Expt [a]		366 nm	
	S_1 [a,b]		375	
2	S_1	2.555	485.3	0.2922
2_LOX-1	S_1	3.256	380.8	0.0043
2_LOX-1	S_3	4.062	305.2	0.2364
2_5-LOX	S_1	3.211	386.1	0.0081

[a] Reference 17; corresponds to 1-(2-hydroxyphenyl)-3-(4-methoxyphenyl)prop-2-en-1-one (methoxy substituent in position 4 instead of methyl). [b] Calculated at the B3LYP/6-311++G(d,p) level.

Table 6. The λ (nm), energy differences ΔE (eV), and f-values of the $S_1 \rightarrow S_0$ de-excitations of the emission spectra of the free compounds obtained using the B3LYP/def2-SVP method.

	ΔE	λ	f
1	2.328	532.5	0.0000
[a]	2.871	431.9	0.0030
	3.677	337.2	0.5410
2	2.379	521.0	0.1712
[a]	2.699	459.4	0.0299

[a] $S_3 \rightarrow S_0$ de excitations.

The ultraviolet-visible (UV–vis) absorption spectra of hydroxy- and methoxy-substituted chalcones typically exhibit two primary bands: a prominent one in the 340–390 nm range and a secondary one between 220–270 nm [49]. In a recent investigation involving experimental and computational analysis of various chalcone analogs, the compound 1-(2-hydroxyphenyl)-3-(4-methoxyphenyl)prop-2-en-1-one, featuring a methoxy substituent at the 4-position, was examined [49]. Its primary absorption maximum was recorded experimentally at 366 nm and

computed at 375 nm, aligning closely with the predicted value of 384 nm for compound 1 in the current study, which bears a methyl substituent at position 4; refer to **Table 5.**

For the compounds under investigation here, the principal UV–vis absorption maxima for 1 and 2 appeared at 384 nm and 485 nm, respectively, revealing a substantial difference of approximately 100 nm. This indicates that replacing the methyl group with a chlorine atom, acting as an electron-donating substituent, leads to a notable blue shift in the primary band. Notably, the absorption maximum of 2 falls within the blue spectral region, which is relatively uncommon among chalcones. The excitation at 485 nm corresponds to π–π* transitions within the conjugated framework of the chalcone scaffold.

The UV–vis absorption profiles of the encapsulated forms were determined using optimized geometries derived from molecular dynamics simulations of the complexes with 5-LOX and LOX-1. In the case of both compounds bound to 5-LOX, the initial absorption band for the encapsulated version remained near 386 nm, closely matching that of the unbound compound 1. However, encapsulation of chalcone 2 by 5-LOX induced a pronounced blue shift. Within LOX-1, the primary absorption band shifted to 403 nm for encapsulated 1 and to 380 nm for encapsulated 2. These alterations in the lowest-energy absorption bands arise from interactions between the chalcone molecules and the respective enzymes, 5-LOX and LOX-1. In general, the energy gaps for the S0→S1 transitions in the encapsulated chalcones spanned 3.08 to 3.26 eV.

As shown in the UV–vis emission spectra **(Figure 11)**, the primary S1→S0 fluorescence emissions for compounds 1 and 2 occurred at 533 nm and 521 nm, respectively. For compound 1, however, the oscillator strength of this transition was zero, and instead, it displayed a strong emission band at 337 nm. Organic molecules exhibiting fluorescence in this wavelength range hold potential as fluorescent probes and markers for applications in biological imaging, diagnostics, and tagging [50, 51]. Such compounds can be linked to biomolecules or nanoparticles to target and visualize specific cellular components or biomarkers [52]. This computational investigation will be extended in future work. A deeper comprehension of chalcones' electronic properties is crucial for elucidating substituent effects, given that absorption maxima are influenced by the electronic characteristics of these groups. Upcoming computational analyses will explore the impact of UV–vis absorption and emission properties in enzyme-encapsulated chalcone derivatives at active sites, with the goal of identifying promising candidates for biological imaging, diagnostics, and labeling purposes.

The molecular orbitals contributing to the key UV–vis absorption and fluorescence transitions are depicted in **Figure 12**. In the absorption processes, the HOMO and LUMO of the ground state are primarily distributed across the aromatic rings. For compound 1, the HOMO is concentrated on one aromatic ring, whereas the LUMO extends over the ring adjacent to the methyl group. In the unbound chalcone 2, the HOMO resides on the chlorine-bearing aromatic ring, but upon complexation, it shifts to the opposite ring. Across all instances, the LUMO is delocalized throughout the entire molecule, reflecting influences from molecular geometry and the surrounding electronic environment. For emission, the HOMO distribution differs from that in absorption, localizing on the alternate ring, while the LUMO remains spread across the molecule, consistent with absorption patterns. Analysis of these frontier orbitals is vital for interpreting electronic structures, conjugation extent, and light-matter interactions, providing foundational insights into reactivity, stability, and optical behavior of organic molecules. Moreover, emission characteristics shed light on excited-state processes and relaxation mechanisms, which are critical for tailoring compounds with desired photophysical properties.

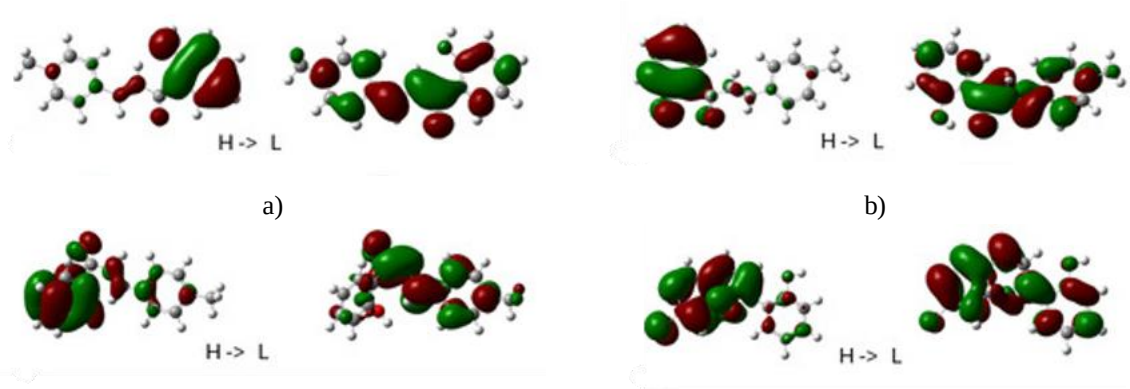

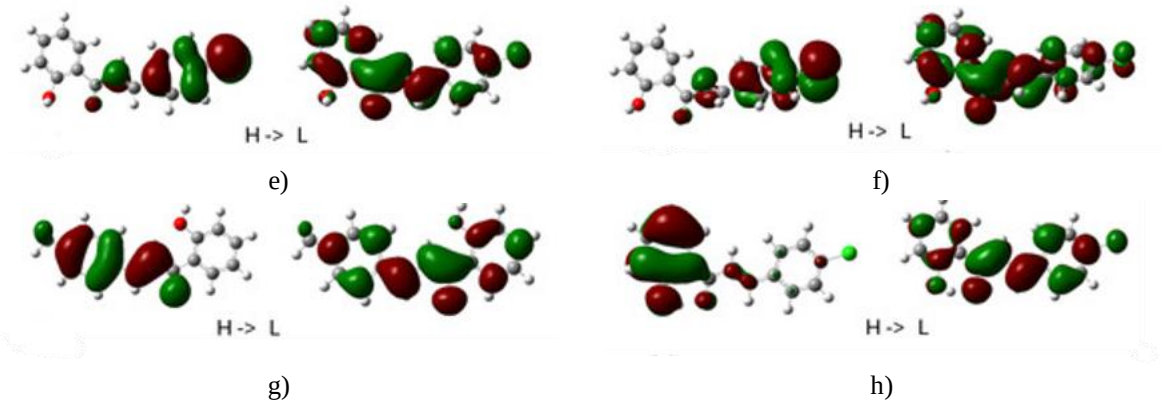

e) f)

g) h)

Figure 12. Frontier molecular orbitals (with HOMO depicted on the left and LUMO on the right) that contribute to the primary S_1 absorption transitions for: (a) unbound compound 1, (b) compound 1 in complex with 5-LOX, (c) compound 1 in complex with LOX-1 following molecular dynamics optimization, (d) unbound compound 2, (e) compound 2 in complex with 5-LOX, and (f) compound 2 in complex with LOX-1. Additionally, the frontier molecular orbitals associated with the $S_1 \rightarrow S_0$ fluorescence transitions are shown for (g) unbound compound 1 and (h) unbound compound 2.

MM/GBSA binding free energy calculations

MM/GBSA binding free energy calculations were performed on the most representative protein–ligand complexes identified through clustering analysis of the trajectories from Desmond molecular dynamics simulations. The results indicate that compound 1 exhibits stronger and more selective binding to the 5-LOX enzyme, with a calculated ΔG_bind of −43.90 kcal/mol. As evident from **Table 7**, both compounds demonstrate more favorable binding affinities toward 5-LOX compared to the other enzymes studied, which is consistent with the trends observed in the docking scores.

Table 7. MM/GBSA values.

Compound_Enzyme	ΔG_Bind Value (kcal/mol)
1_15-LOX	−35.90
2_15-LOX	−27.32
1_5-LOX	−43.90
2_5-LOX	−31.07
1-LOX-1	−34.49
2-LOX-1	−23.80

In vitro assessment of the compounds' inhibitory activity against human 15-LOX-1 and lipoxidase enzymes

To conclude the experimental evaluation, the inhibitory effects of the synthesized compounds were tested against human 15-LOX-1 and lipoxidase, both members of the lipoxygenase (LOX) enzyme family. The primary objective was to determine the compounds' selectivity profiles and detect any inhibitory activity at micromolar concentrations (100 μM). As illustrated in **Figure 13**, the compounds displayed only slight inhibitory effects, suggesting some degree of binding to the target proteins. Nevertheless, none of the compounds demonstrated substantial potency, with residual enzyme activity exceeding 85% for both enzymes. ThioLox, a established inhibitor of human 15-LOX-1, served as the positive control [43]. These findings align with the saturation transfer difference (STD) NMR results, where no distinct peaks were detected for LOX-1.

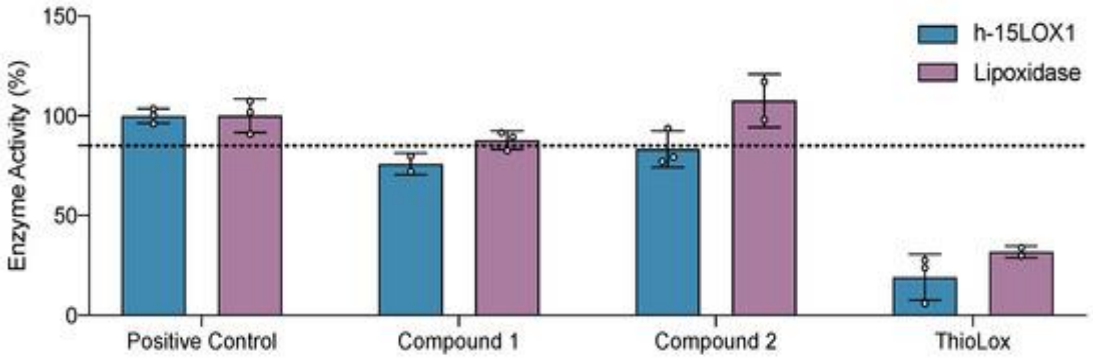

Figure 13. Activity of the evaluated compounds (at 100 μM) toward human 15-LOX-1 and soybean lipoxygenase.

The positive control (no inhibitor present) was normalized to 100% activity (dashed line corresponds to 85%). Mean values and standard deviations from replicate experiments are shown.

Discrepancies observed between computational docking predictions and the modest inhibitory activity in enzyme assays can arise from multiple factors. Computational models primarily evaluate predicted binding energies but frequently fail to account for real-world biological factors, including compound solubility, chemical stability, and dynamic conformational changes in the enzyme. Furthermore, assay-specific variables—such as buffer pH, suboptimal ligand positioning, or steric clashes within the binding pocket—may diminish observed activity. Potential limitations in assay protocol or errors during compound handling could also explain these differences.

Conclusion

The present study centers on determining and examining the molecular structures of two biologically active molecules by integrating NMR spectroscopic techniques with computational modeling. Interactions at the atomic level were revealed through the application of Saturation Transfer Difference NMR (STD NMR), a method that detects ligand binding to target macromolecules. These experimental observations aligned well with the structural predictions derived from theoretical calculations.

Virtual screening and simulations involved 5-LOX, 15-LOX, and LOX-1 enzymes. Findings indicated robust binding interactions of the molecules with 5-LOX and LOX-1, and molecular dynamics simulations showed that the ligands persisted within the active sites of these proteins. Evaluation via the SwissADME tool revealed that all analogs lacked hepatotoxicity and adhered to Lipinski's Rule of Five. Such properties position them as promising, non-toxic candidates with therapeutic potential across multiple biological and drug-related applications. The work offers useful guidance for organic chemists designing novel scaffolds tailored to particular targets. Overall, the goal is to leverage computational docking and screening strategies to guide the creation of compounds with selectivity for designated biomolecular systems.

Acknowledgments: None

Conflict of Interest: None

Financial Support: None

Ethics Statement: None

References

1. Qin HL, Zhang ZW, Lekkala R, Alsulami H, Rakesh KP. Chalcone hybrids as privileged scaffolds in antimalarial drug discovery: A key review. Eur J Med Chem. 2020;193:112215.
2. Papaemmanouil C, Chatziathanasiadou MV, Chatzigiannis C, Chontzopoulou E, Mavromoustakos T, Grdadolnik SG, et al. Unveiling the interaction profile of rosmarinic acid and its bioactive substructures with serum albumin. J Enzyme Inhib Med Chem. 2020;35:786–804.

3. Detsi A, Majdalani M, Kontogiorgis CA, Hadjipavlou-Litina D, Kefalas P. Natural and synthetic 2′-hydroxy-chalcones and aurones: Synthesis, characterization and evaluation of the antioxidant and soybean lipoxygenase inhibitory activity. Bioorg Med Chem. 2009;17:8073–85.
4. Kostopoulou I, Tzani A, Polyzos NI, Karadendrou MA, Kritsi E, Pontiki E, et al. Exploring the 2′-hydroxy-chalcone framework for the development of dual antioxidant and soybean lipoxygenase inhibitory agents. Molecules. 2021;26:2777.
5. Fu Y, Liu D, Zeng H, Ren X, Song B, Hu D, et al. New chalcone derivatives: Synthesis, antiviral activity and mechanism of action. RSC Adv. 2020;10:24483–90.
6. Nowakowska Z. A review of anti-infective and anti-inflammatory chalcones. Eur J Med Chem. 2007;42:125–37.
7. Rosa GP, Seca AML, Barreto MD, Silva AMS, Pinto DCGA. Chalcones and Flavanones Bearing Hydroxyl and/or Methoxyl Groups: Synthesis and Biological Assessments. Appl Sci. 2019;9:2846.
8. Tran TD, Park H, Kim HP, Ecker GF, Thai KM. Inhibitory activity of prostaglandin E2 production by the synthetic 2′-hydroxychalcone analogues: Synthesis and SAR study. Bioorg Med Chem Lett. 2009;19:1650–3.
9. Pande AN, Biswas S, Reddy ND, Jayashree BS, Kumar N, Rao CM. In vitro and in vivo anticancer studies of 2′-hydroxy chalcone derivatives exhibit apoptosis in colon cancer cells by HDAC inhibition and cell cycle arrest. EXCLI J. 2017;16:448.
10. Kuhn H, Banthiya S, Van Leyen K. Mammalian lipoxygenases and their biological relevance. Biochim Biophys Acta Mol Cell Biol Lipids. 2015;1851:308–30.
11. Georgiou N, Chontzopoulou E, Cheilari A, Katsogiannou A, Karta D, Vavougyiou K, et al. Thiocarbohydrazone and chalcone-derived 3,4-dihydropyrimidinethione as lipid peroxidation and soybean lipoxygenase inhibitors. ACS Omega. 2023;8:11966–77.
12. Tzani A, Kritsi E, Tsamantioti L, Kostopoulou I, Karadendrou MA, Zoumpoulakis P, et al. Synthesis, Conformational Analysis and ctDNA Binding Studies of Flavonoid Analogues Possessing the 3,5-di-tert-butyl-4-hydroxyphenyl Moiety. Antioxidants. 2022;11:2273.
13. Lin YM, Zhou Y, Flavin MT, Zhou LM, Nie W, Chen FC. Chalcones and flavonoids as anti-tuberculosis agents. Bioorg Med Chem. 2002;10:2795–802.
14. Georgiou N, Katsogiannou A, Skourtis D, Iatrou H, Tzeli D, Vassiliou S, et al. Conformational Properties of New Thiosemicarbazone and Thiocarbohydrazone Derivatives and Their Possible Targets. Molecules. 2022;27:2537.
15. Georgiou N, Gouleni N, Chontzopoulou E, Skoufas GS, Gkionis A, Tzeli D, et al. Structure assignment, conformational properties and discovery of potential targets of the Ugi cinnamic adduct NGI25. J Biomol Struct Dyn. 2023;41:1253–66.
16. Abraham RJ, Mobli M. The prediction of 1H NMR chemical shifts in organic compounds. Spectrosc Eur. 2004;16:16–22.
17. Bifulco G, Dambruoso P, Gomez-Paloma L, Riccio R. Determination of relative configuration in organic compounds by NMR spectroscopy and computational methods. Chem Rev. 2007;107:3744–79.
18. Elyashberg M. Identification and structure elucidation by NMR spectroscopy. TrAC Trends Anal Chem. 2015;69:88–97.
19. Chontzopoulou E, Papaemmanouil CD, Chatziathanasiadou MV, Kolokouris D, Kiriakidi S, Konstantinidi A, et al. Molecular investigation of artificial and natural sweeteners as potential anti-inflammatory agents. J Biomol Struct Dyn. 2022;40:12608–20.
20. Hall JL, Sohail A, Cabrita EJ, Macdonald C, Stockner T, Sitte HH, et al. Saturation transfer difference NMR on the integral trimeric membrane transport protein GltPh determines cooperative substrate binding. Sci Rep. 2020;10:16483.
21. Viegas A, Manso J, Nobrega FL, Cabrita EJ. Saturation-transfer difference (STD) NMR: A simple and fast method for ligand screening and characterization of protein binding. J Chem Educ. 2011;88:990–4.
22. van Mourik T, Bühl M, Gaigeot MP. Density functional theory across chemistry, physics and biology. Philos Trans R Soc A Math Phys Eng Sci. 2014;372:20120488.
23. Grimme S, Antony J, Ehrlich S, Krieg H. A consistent and accurate ab initio parametrization of density functional dispersion correction (DFT-D) for the 94 elements H-Pu. J Chem Phys. 2010;132:154104.

24. Weigend F, Ahlrichs R. Balanced basis sets of split valence, triple zeta valence and quadruple zeta valence quality for H to Rn: Design and assessment of accuracy. Phys Chem Chem Phys. 2005;7:3297.
25. Neese F, Wennmohs F, Becker U, Riplinger C. The ORCA quantum chemistry program package. J Chem Phys. 2020;152:224108.
26. Dubé D, Blouin M, Brideau C, Chan CC, Desmarais S, Ethier D, et al. Quinolines as potent 5-lipoxygenase inhibitors: Synthesis and biological profile of L-746,530. Bioorg Med Chem Lett. 1998;8:1255–60.
27. Offenbacher AR, Hu S, Poss EM, Carr CAM, Scouras AD, Prigozhin DM, et al. Hydrogen–Deuterium Exchange of Lipoxygenase Uncovers a Relationship between Distal, Solvent Exposed Protein Motions and the Thermal Activation Barrier for Catalytic Proton-Coupled Electron Tunneling. ACS Cent Sci. 2017;3:570–9.
28. Choi J, Chon JK, Kim S, Shin W. Conformational flexibility in mammalian 15S-lipoxygenase: Reinterpretation of the crystallographic data. Proteins Struct Funct Bioinforma. 2008;70:1023–32.
29. Gilbert NC, Bartlett SG, Waight MT, Neau DB, Boeglin WE, Brash AR, et al. The Structure of Human 5-Lipoxygenase. Science. 2011;331:217–9.
30. Schrodinger LLC. MacroModel, Version 10.2. New York, NY: Schrodinger LLC; 2013.
31. Jorgensen WL, Maxwell DS, Tirado-Rives J. Development and testing of the OPLS all-atom force field on conformational energetics and properties of organic liquids. J Am Chem Soc. 1996;118:11225–36.
32. Imtiaz S, Muzaffar S, Ali SM. Demonstrating accuracy of the already proposed protocol for structure elucidation of cyclodextrin inclusion complexes by validation using quantitative ROESY analysis. J Incl Phenom Macrocycl Chem. 2021;100:71–87.
33. Essmann U, Perera L, Berkowitz ML, Darden T, Lee H, Pedersen LG. A smooth particle mesh Ewald method. J Chem Phys. 1995;103:8577.
34. Martyna GJ, Tobias DJ, Klein ML. Constant pressure molecular dynamics algorithms. J Chem Phys. 1994;101:4177–89.
35. Humphreys DD, Friesner RA, Berne BJ. A multiple-time-step Molecular Dynamics algorithm for macromolecules. J Phys Chem. 1994;98:6885–92.
36. Lyman E, Zuckerman DM. Ensemble-based convergence analysis of biomolecular trajectories. Biophys J. 2006;91:164–72.
37. Bütikofer A, Løken KV, Salvanes KG. Infant health care and long-term outcomes. Rev Econ Stat. 2019;101:341–54.
38. Lee C, Yang W, Parr RG. Development of the Colle-Salvetti correlation-energy formula into a functional of the electron density. Phys Rev B. 1988;37:785–9.
39. Becke AD. A new mixing of Hartree–Fock and local density-functional theories. J Chem Phys. 1993;98:1372–7.
40. Tzeli D, Theodorakopoulos G, Petsalakis ID, Ajami D, Rebek J. Conformations and Fluorescence of Encapsulated Stilbene. J Am Chem Soc. 2012;134:4346–54.
41. Frisch MJD, Trucks GW, Schlegel HB, Scuseria GE, Robb MA, Cheeseman JR, et al. Gaussian 16, Revision B.01. Wallingford, CT: Gaussian, Inc.; 2016.
42. Pattar SV, Adhoni SA, Kamanavalli CM, Kumbar SS. In silico molecular docking studies and MM/GBSA analysis of coumarin-carbonodithioate hybrid derivatives divulge the anticancer potential against breast cancer. Beni-Suef Univ J Basic Appl Sci. 2020;9:36.
43. Eleftheriadis N, Poelman H, Leus NGJ, Honrath B, Neochoritis CG, Dolga A, et al. Design of a novel thiophene inhibitor of 15-lipoxygenase-1 with both anti-inflammatory and neuroprotective properties. Eur J Med Chem. 2016;122:786–801.
44. Spacho N, Casertano M, Imperatore C, Papadopoulos C, Menna M, Eleftheriadis N. Investigating the Catalytic Site of Human 15-Lipoxygenase-1 via Marine Natural Products. Chem Eur J. 2024;30:e202402279.
45. Jantan I, Bukhari SNA, Adekoya OA, Sylte I. Studies of synthetic chalcone derivatives as potential inhibitors of secretory phospholipase A2, cyclooxygenases, lipoxygenase and pro-inflammatory cytokines. Drug Des Devel Ther. 2014;8:1405–18.
46. Zeraik ML, Pauli I, Dutra LA, Cruz RS, Valli M, Paracatu LC, et al. Identification of a Prenyl Chalcone as a Competitive Lipoxygenase Inhibitor: Screening, Biochemical Evaluation and Molecular Modeling Studies. Molecules. 2021;26:2205.

47. Mayer M, Meyer B. Characterization of Ligand Binding by Saturation Transfer Difference NMR Spectroscopy. Angew Chem Int Ed. 1999;38:1784–8.
48. Georgiou N, Tzani A, Vavougyiou K, Papadopoulos C, Eleftheriadis N, Šket P, et al. A Study of the Potential Anti-Inflammatory Drugs Chalcone Derivatives through the Combination of NMR Spectroscopy and Molecular Modeling [Internet]. Preprint.org. 2024. Available from: https://www.preprints.org/manuscript/202411.0126/v1 [cited 2024 Dec 11].
49. Abbo HS, Hung Lai C, Titinchi SJJ. Substituent and solvent effects on UV-visible absorption spectra of chalcones derivatives: Experimental and computational studies. Spectrochim Acta Part A Mol Biomol Spectrosc. 2023;303:123180.
50. Snaith HJ. Perovskites: The Emergence of a New Era for Low-Cost, High-Efficiency Solar Cells. J Phys Chem Lett. 2013;4:3623–30.
51. Ethirajan M, Chen Y, Joshi P, Pandey RK. The role of porphyrin chemistry in tumor imaging and photodynamic therapy. Chem Soc Rev. 2011;40:340–62.
52. Weissleder R. A clearer vision for in vivo imaging. Nat Biotechnol. 2001;19:316–7.